

Channel Charting in Real-World Coordinates with Distributed MIMO

Sueda Taner, Victoria Palhares, and Christoph Studer

Abstract—Channel charting is an emerging self-supervised method that maps channel-state information (CSI) to a low-dimensional latent space (the channel chart) that represents pseudo-positions of user equipments (UEs). While channel charts preserve local geometry, i.e., nearby UEs are nearby in the channel chart (and vice versa), the pseudo-positions are in arbitrary coordinates and global geometry is typically not preserved. In order to embed channel charts in real-world coordinates, we first propose a bilateration loss for distributed multiple-input multiple-output (D-MIMO) wireless systems in which only the access point (AP) positions are known. The idea behind this loss is to compare the received power at pairs of APs to determine whether a UE should be placed closer to one AP or the other in the channel chart. Second, we propose a line-of-sight (LoS) bounding-box loss that places the UE in a predefined LoS area of each AP that is estimated to have a LoS path to the UE. We demonstrate the efficacy of combining both of these loss functions with neural-network-based channel charting using ray-tracing-based and measurement-based channel vectors. Our approach outperforms several baselines and maintains the self-supervised nature of channel charting as it does not rely on geometrical propagation models or require ground-truth UE position information.

I. INTRODUCTION

Channel charting is a self-supervised method that extracts user equipment (UE) pseudo-position solely by processing estimated channel-state information (CSI) at infrastructure basestations (BSs) or access points (APs) [3]. The key idea is to apply dimensionality reduction to a large database of CSI features that represent large-scale fading properties of the wireless channel, such as time-of-arrival (ToA), angle-of-arrival (AoA), power-delay profile, etc. The low-dimensional latent space resulting from dimensionality reduction is the so-called *channel chart*, which is tied to UE position. More specifically, UEs nearby in real space are nearby in the channel chart and vice versa. The learned channel chart can be used to assist a wide range of applications in wireless systems that rely on UE position information, such as pilot allocation [4], beam

management [5], [6], channel capacity prediction [7], and many more; see [8] for an overview.

Although channel charts preserve the local geometry of UE positions, i.e., nearby UEs correspond to points that are nearby in the channel chart (and the other way around), global geometry is typically distorted, e.g., scaled, rotated, and warped. Furthermore, the learned channel charts are represented in arbitrary coordinates, which is a direct consequence of self-supervised learning. Multipoint channel charting techniques, which process CSI acquired at multiple distributed multi-antenna APs, have been shown to improve global geometry [9]–[11]. Nonetheless, the resulting channel charts remain to be pseudo-positions with no ties to real-world coordinates. In this paper, we resolve exactly this limitation: We aim to learn channel charts that are interpretable in terms of real-world coordinates.

A. Contributions

We propose novel methods that learn neural-network-based channel charting functions in a distributed multiple-input multiple-output (D-MIMO) scenario to generate channel charts in real-world coordinates. Our key contributions are as follows: We generalize our bilateration loss put forward in [1] from conditions where the UEs have line-of-sight (LoS) paths to all APs to more realistic conditions where some APs may be in non-LoS. The bilateration loss compares the receive power at pairs of APs to place the UE closer to the AP that is receiving higher power; here, we introduce a power threshold that eliminates non-LoS APs from being included in the bilateration loss. We furthermore propose a novel LoS bounding-box loss, which places the UE in the LoS area of the APs whose receive power is above the aforementioned power threshold. While the bilateration loss relies on at least two LoS APs, the LoS bounding-box loss also applies to UEs with LoS connectivity to only one AP. We propose to combine the bilateration and the LoS bounding-box losses with the timestamp-based triplet loss from [12] for improved channel chart quality. We demonstrate the efficacy of our method using channel vectors from a commercial ray-tracer [13] for an indoor and an outdoor scenario, and for one indoor scenario with measured channel vectors [2]. We emphasize that the proposed methods are weakly supervised as they only require (i) knowledge of the AP positions and (ii) approximate knowledge of the LoS areas surrounding each AP—*no* geometric models, accurate AP synchronization, or labeled CSI samples with UE ground-truth positions are required.

S. Taner, V. Palhares, and C. Studer are with the Department of Information Technology and Electrical Engineering, ETH Zurich, Switzerland (taners@iis.ee.ethz.ch, vmenesca@ethz.ch, and studer@ethz.ch).

The work of ST, VP, and CS was supported in part by an ETH Research Grant, by the Swiss National Science Foundation (SNSF) grant 200021_207314, and by CHIST-ERA grant for the project CHASER (CHIST-ERA-22-WAI-01) through the SNSF grant 20CH21_218704.

The authors thank Remcom for providing a license for the Wireless InSite ray-tracing software. The authors also thank Olav Tirkkonen and Maxime Guillaud for discussions on channel charting in real-world coordinates.

A preliminary version of this work was presented at the 2023 IEEE GLOBECOM [1]. In [1], the bilateration loss was proposed for channel charting in real-world coordinates for line-of-sight (LoS) scenarios. Here, we extend our approach to mixed LoS and non-LoS scenarios by modifying the bilateration loss and by introducing a novel LoS bounding-box loss. In addition, we include experimental results with measured channel vectors from [2].

B. Relevant Prior Art

The literature describes a plethora of methods for radio-based positioning [14]–[17]. While our main goal is not accurate positioning, we briefly review these methods for completeness. Geometric model-based positioning methods, e.g., methods that rely on ToA and/or AoA (see [18] and the references therein), can achieve precise positioning in environments with LoS connectivity. These methods, however, rely on accurately synchronized APs, and their performance degrades in non-LoS and multipath scenarios. An alternative radio-based positioning technique which does not require AP synchronization is fingerprinting [19]–[28]. CSI fingerprinting methods rely on the offline collection of a large CSI database where the ground-truth UE position corresponding to each CSI sample must be known. However, this approach is costly since setting up a ground-truth reference system is both cumbersome and expensive; moreover, the ground-truth labeled CSI measurement campaign needs to be repeated whenever there is a significant change in the physical environment.

In order to reduce the number of ground-truth labeled CSI samples required by fingerprinting-based methods, semi-supervised learning methods have been proposed [29]–[33]. This strain of methods assumes that the ground-truth UE positions are known for a (small) subset of the training dataset, and incorporates these known positions into learning a channel charting function. In contrast to such approaches, which still require a ground-truth reference positioning system, our method does not require ground-truth position information for the CSI samples.

More recently, another strain of methods that incorporates real-world positions directly into channel charting has been proposed in [34]–[36]. Reference [34] relies on several zone-labeled CSI samples to predict a zone for every CSI sample; this zone information is then used during weakly-supervised training. References [35], [36] propose loss functions that leverage estimated ToA or AoA to assist channel charting. As we have mentioned before, these approaches require accurately synchronized APs. In contrast, we require neither zone-labeled CSI samples nor accurate AP synchronization.

Several methods have been proposed that first create a channel chart in a self-supervised manner, then use an affine transform that maps the channel chart to real-world positions [35], [37]–[40]. Various methods have been proposed to learn such affine transforms: The method in [37] estimates the AP positions in the channel chart and maps these positions to the real-world positions of the APs. The method in [39] assumes that a map of the environment is known a priori and aims to match the channel chart to this environment map. The methods in [38], [40] use several ground-truth UE positions¹, and the method in [35] uses UE position estimates obtained through geometric model-based positioning techniques. In contrast to such transformation-based methods, which would fail when channel charts have non-affine distortions of the real-world positions and may require labeled CSI samples, we aim to

¹We make a distinction between methods that use ground-truth positions *during* neural-network training [19]–[33] and methods that use ground-truth positions *after* training [38], [40]. We only use the terms “supervised” and “semi-supervised” to refer to the first kind of methods.

directly learn channel charts that are embedded in real-world coordinates in a weakly-supervised manner.

C. Notation

Column vectors and matrices are denoted by lowercase and uppercase boldface letters, respectively; sets are denoted by uppercase calligraphic letters. The column-wise vectorization of \mathbf{A} is denoted by $\text{vec}(\mathbf{A})$. For a vector \mathbf{a} , the Euclidean norm is $\|\mathbf{a}\|$ and the entry-wise absolute value is $|\mathbf{a}|$; for a matrix \mathbf{A} , the Frobenius norm is $\|\mathbf{A}\|_F$. The operator $(x)^+ = \max\{x, 0\}$ is the rectified linear unit (ReLU). The indicator function is denoted by $\mathbb{1}_{\{c\}}$, which is one if the condition c is met and zero otherwise.

D. Paper Outline

The rest of the paper is organized as follows. Sec. II introduces the basics of channel charting. Sec. III proposes novel loss functions that embed channel charts in real-world coordinates. Sec. IV details the proposed methods, baselines, and performance metrics. Sec. V presents simulation results for three different scenarios. Sec. VI concludes the paper.

II. CHANNEL CHARTING BASICS

We now briefly outline the basics of channel charting, detail the system model, and discuss parametric channel charting with neural networks using the triplet-based learning approach [12], which is part of the method we propose in Sec. III.

A. Operating Principle

Channel charting typically operates in two phases [3]. In the first phase, CSI from a large number of different UE positions is acquired and CSI features that capture large-scale fading properties of the wireless channel are stored in a database. By applying parametric dimensionality reduction [41] to the CSI feature database, one then learns a channel charting function (e.g., implemented as a neural network), which maps CSI features to a low-dimensional representation: the channel chart. Channel charts have the useful property that the UEs transmitting from nearby positions are also placed nearby in the channel chart and vice versa. We reiterate that channel-chart learning is self-supervised, meaning that no ground-truth information about the UEs’ position is required. In the second phase, the channel charting function is used to map new CSI features to points in the channel chart, which represent the transmitting UEs’ pseudo-positions.

B. System Model

We consider a D-MIMO wireless system in which one or multiple single-antenna UEs transmit pilots to A distributed APs with M_R antennas each, leading to $B = AM_R$ receive antennas in total. We consider orthogonal frequency division multiplexing (OFDM) transmission with W occupied subcarriers. We assume that the AP $a \in \mathcal{A} = \{1, \dots, A\}$ is at position $\mathbf{x}^{(a)} \in \mathbb{R}^3$ in physical space, and that these positions are known. Moreover, we assume approximate knowledge of the minimum

and maximum x and y coordinates of the LoS area for each AP², denoted by $x_{\min}^{(a)}, x_{\max}^{(a)}, y_{\min}^{(a)}, y_{\max}^{(a)} \in \mathbb{R}$. Therefore, we have a rectangular bounding box encompassing the LoS area. We denote the LoS bounding box for AP a by

$$\mathcal{B}^{(a)} = \{(x, y) \in \mathbb{R}^2 : x \in [x_{\min}^{(a)}, x_{\max}^{(a)}], y \in [y_{\min}^{(a)}, y_{\max}^{(a)}]\}. \quad (1)$$

Suppose that we have N pilot transmissions from one UE at (unknown) positions $\mathbf{x}^{(n)} \in \mathbb{R}^3$ at timestamps t_n for $n \in \mathcal{N} = \{1, \dots, N\}$. The n th transmission from UE position $\mathbf{x}^{(n)}$ enables the AP a to estimate the associated CSI vector $\mathbf{h}_w^{(n,a)} \in \mathbb{C}^{M_R}$ at timestamp t_n and subcarrier w . By stacking the channel vectors $\{\mathbf{h}_w^{(n,a)}\}_{a=1}^A$ from all APs, we can construct a CSI vector $\mathbf{h}_w^{(n)} \in \mathbb{C}^B$ that contains CSI for all B receive antennas at subcarrier w . It is important to note that we do not require the A APs to be perfectly synchronized while acquiring CSI; the only requirement is that the CSI estimated at each AP belongs to the same UE transmitting from approximately the same position $\mathbf{x}^{(n)}$ at approximately the same timestamp t_n . Finally, we concatenate the channel vectors from all subcarriers to construct a $B \times W$ CSI matrix associated with the UE at timestamp t_n as $\mathbf{H}^{(n)} = [\mathbf{h}_1^{(n)}, \dots, \mathbf{h}_W^{(n)}]$. The entire CSI database is given by the set of matrices $\{\mathbf{H}^{(n)}\}_{n \in \mathcal{N}}$.

C. CSI Feature Extraction

In order to be agnostic to small-scale fading effects and resilient to system and hardware impairments (e.g., phase offsets between APs), we extract large-scale fading properties of the wireless channel by transforming the estimated CSI matrices into CSI features [3], [12], [25]. In what follows, we utilize the CSI features from [21], [30]. First, we transform frequency-domain CSI into the (approximate) delay domain by applying an inverse discrete Fourier transform over the W occupied subcarriers. Since most of the received power should be concentrated on the first few taps, we truncate the delay-domain CSI matrix by taking its first $C \ll W$ columns; we denote the truncated delay-domain CSI matrix by $\hat{\mathbf{H}}^{(n)} \in \mathbb{C}^{B \times C}$. We vectorize this matrix to $\hat{\mathbf{h}}^{(n)} = \text{vec}(\hat{\mathbf{H}}^{(n)}) \in \mathbb{C}^{D'}$, where $D' = BC$. Finally, we compute the unit-norm CSI feature vector $\mathbf{f}^{(n)} \in \mathbb{R}^{D'}$ as

$$\mathbf{f}^{(n)} = \frac{|\hat{\mathbf{h}}^{(n)}|}{\|\hat{\mathbf{h}}^{(n)}\|}, \quad (2)$$

which ignores (i) phase shifts (e.g., stemming from APs that are not accurately synchronized) by taking the entry-wise absolute value and (ii) the UEs' transmit power (e.g., as the UEs can set their own transmit power) by normalizing the resulting vector. The entire CSI feature dataset is then given by the set of CSI feature vectors $\{\mathbf{f}^{(n)}\}_{n \in \mathcal{N}}$.

D. Channel Charting with Neural Networks

With the CSI feature database, one can then learn a channel-charting function $g_\theta : \mathbb{R}^{D'} \rightarrow \mathbb{R}^D$, which maps a CSI feature vector $\mathbf{f}^{(n)}$ to a D -dimensional pseudo-position in the channel

chart as follows: $\hat{\mathbf{x}}^{(n)} = g_\theta(\mathbf{f}^{(n)})$. In this paper, we implement the function g_θ as a neural network that is parametrized by the vector θ which includes all of the weights and biases. While real-world positions are in three-dimensional space with coordinates (x, y, z) , the channel chart can be embedded in fewer dimensions if, for example, the z -coordinate is fixed across the AP and UE positions. Hence, assuming that $D \leq 3$, we denote the truncated vector consisting of the first D entries of $\mathbf{x}^{(n)}$ and $\underline{\mathbf{x}}^{(a)}$ as $\tilde{\mathbf{x}}^{(n)} \in \mathbb{R}^D$ and $\tilde{\mathbf{x}}^{(a)} \in \mathbb{R}^D$, respectively.

The literature describes a variety of methods to learn neural-network-based channel charting functions, such as autoencoders [3], [29], Siamese neural networks [30], and neural networks trained with a timestamp-based triplet-loss [12], [42], [43]. In what follows, we focus on the timestamp-based triplet-loss approach from [12].

E. Triplet-Based Channel Charting

Assuming that the timestamps associated with all CSI features are available, reference [12] proposes to use this side information when comparing pairwise distances in latent space. To this end, one defines a set of triplets from the set of sample indices \mathcal{N} as follows:

$$\mathcal{T} = \{(n, c, f) \in \mathcal{N}^3 : 0 < |t_n - t_c| \leq T_c < |t_n - t_f|\}, \quad (3)$$

where $T_c > 0$ is a coherence-time parameter that categorizes the CSI features as close or far in time. If t_n is closer to t_c than t_f , then we would expect the Euclidean distance between the UE positions at timestamp t_n and t_c to be smaller than that of t_f . This property can be expressed with the following triplet loss [12]:

$$\mathcal{L}_t = \frac{1}{|\mathcal{T}|} \sum_{(n,c,f) \in \mathcal{T}} (\|g_\theta(\mathbf{f}^{(n)}) - g_\theta(\mathbf{f}^{(c)})\| - \|g_\theta(\mathbf{f}^{(n)}) - g_\theta(\mathbf{f}^{(f)})\| + M_t)^+. \quad (4)$$

Here, the margin parameter $M_t \geq 0$ enforces $g_\theta(\mathbf{f}^{(n)})$ to be at least M_t closer to $g_\theta(\mathbf{f}^{(c)})$ than to $g_\theta(\mathbf{f}^{(f)})$.

As demonstrated in [12], one can train a neural network that implements the channel charting function g_θ by minimizing the loss \mathcal{L}_t ; this approach is self-supervised as the loss only utilizes the training dataset without any additional ground-truth labels, such as UE positions. We reiterate that the coordinate system of the resulting channel chart is arbitrary (e.g., scaled, rotated, and globally warped). The methods we propose next address exactly this limitation of existing channel charting pipelines.

III. CHANNEL CHARTING IN REAL-WORLD COORDINATES

We now propose two loss functions that enable one to directly learn channel charts in real-world coordinates. Our first loss function uses the known AP positions in a D-MIMO scenario. Our second loss relies on known bounding boxes for the LoS area surrounding each AP. We reiterate that *no* geometric models, accurate time synchronization among APs, or CSI samples labeled with UE positions are required.

Both of the loss functions we propose rely on LoS APs. Hence, we have the following simple procedure to estimate whether an AP has a LoS or non-LoS channel with the n th

²It is a reasonable assumption to know the AP positions and their LoS areas (e.g., the room the AP is in), as the APs are typically not placed arbitrarily but according to a carefully-crafted deployment plan.

UE position: Let $\hat{\mathbf{H}}^{(n,a)} \in \mathbb{C}^{M_R \times C}$ denote the submatrix of $\hat{\mathbf{H}}^{(n)}$ which consists of the M_R rows corresponding to AP a . We compute the receive power associated with the UE and the a th AP as $P^{(n,a)} = 20 \log_{10}(\|\hat{\mathbf{H}}^{(n,a)}\|_F)$, $a \in \mathcal{A}$. By plotting the values of $P^{(n,a)}$ with respect to t_n , we can observe where the power has an instantaneous, large drop, and manually set a power threshold P_{thr} ; we provide concrete examples for choosing this threshold in Sec. V-B. We classify the APs whose receive power is above this threshold as “in LoS,” and the remaining ones as “not in LoS.” We construct the set of (estimated) LoS APs for each UE position as follows:

$$\tilde{\mathcal{A}}^{(n)} = \{a \in \mathcal{A} : P^{(n,a)} > P_{\text{thr}}\}. \quad (5)$$

We utilize $\tilde{\mathcal{A}}^{(n)}$ in our loss functions detailed next.

A. Bilateralation Loss

Assuming that a UE’s pilot signal is received at multiple APs in the considered D-MIMO scenario, our bilateralation loss aims to utilize the known AP positions and place the UE closer to one AP than another. Here, our CSI-based clue for the real-world position of the UE is the relative power of the CSI matrix for each LoS AP: As one would expect, an AP with higher relative receive power tends to be closer to the UE under LoS conditions, whereas the power would give no clue on the distance under non-LoS conditions. Hence, we only utilize the APs from $\tilde{\mathcal{A}}^{(n)}$ in (5) for the bilateralation loss. Specifically, we define the following set of AP pairs:

$$\mathcal{P}^{(n)} = \{(a_c, a_f) \in (\tilde{\mathcal{A}}^{(n)})^2 : P^{(n,a_c)} > P^{(n,a_f)} + M_p\}. \quad (6)$$

The set $\mathcal{P}^{(n)}$ generates pairs of AP indices (a_c, a_f) , where the two selected APs act as close and far reference points for the n th UE position. Here, the margin parameter $M_p \geq 0$ enforces the set $\mathcal{P}^{(n)}$ to only include AP pairs whose channel powers differ by at least M_p . The assumption that the UE n should be closer to AP a_c than AP a_f as determined by the set $\mathcal{P}^{(n)}$ in (6) leads to the following *bilateralation loss*:

$$\mathcal{L}_{\text{bi}} = \frac{1}{\sum_{n \in \mathcal{N}} |\mathcal{P}^{(n)}|} \sum_{n \in \mathcal{N}} \sum_{(a_c, a_f) \in \mathcal{P}^{(n)}} (\|g_{\theta}(\mathbf{f}^{(n)}) - \tilde{\mathbf{x}}^{(a_c)}\| - \|g_{\theta}(\mathbf{f}^{(n)}) - \tilde{\mathbf{x}}^{(a_f)}\| + M_b)^+. \quad (7)$$

Here, the margin $M_b \geq 0$ enforces $g_{\theta}(\mathbf{f}^{(n)})$ to be at least M_b closer to AP a_c than AP a_f . We emphasize that the loss \mathcal{L}_{bi} requires no assumption of how far each AP should be from the UE based on their channel power; we merely deduce relative distances to the two APs. Moreover, while the underlying assumption on the power-distance relation between UE and APs may not always hold, we seek no such guarantee—this claim is supported with a concrete example in Sec. V-A2.

One can train a neural network that implements the channel charting function g_{θ} by minimizing the loss \mathcal{L}_{bi} in (7); this approach is weakly-supervised as the loss incorporates only partial information on the ground-truth labels (i.e., only position information of the APs is used).

We note that a loss based on received power was also proposed in [34]; this loss, however, compares the power of two CSI vectors corresponding to the channel between one AP

and the UE at two timestamps t_i and t_k in order to deduce whether $\mathbf{x}^{(i)}$ or $\mathbf{x}^{(k)}$ is closer to the AP. This loss does not leverage the fact that multiple APs receive the UE’s pilot signal simultaneously. In contrast, our bilateralation loss in (7) takes each CSI feature into account individually and compares the receive power between a pair of APs; this means that our loss does not rely on timestamps. Thus, our bilateralation loss could also be used in scenarios in which timestamps are irrelevant, e.g., a multiuser scenario with stationary UEs.

While we can utilize the bilateralation loss for UE positions that have a LoS path to at least two APs, the loss function we propose next also targets UEs with only one LoS AP.

B. LoS Bounding-Box Loss

Assume that we have a bounding box as defined in (1) for the LoS area of each AP. The LoS bounding-box loss aims to place the UE inside the LoS bounding box of each AP which is estimated to have a LoS path to the UE. Here, our CSI-based clue to the real-world position of the UE is the receive power at each AP: If the receive power at an AP is sufficiently high, then one would expect the UE to be inside the LoS bounding box of this AP; this leads to the following *LoS bounding-box loss*:

$$\mathcal{L}_{\text{box}} = \frac{1}{\sum_{n=1}^N |\tilde{\mathcal{A}}^{(n)}|} \sum_{n \in \mathcal{N}} \sum_{a \in \tilde{\mathcal{A}}^{(n)}} \ell_a(g_{\theta}(\mathbf{f}^{(n)})). \quad (8)$$

Here, we define $\ell_a(\mathbf{x}) : \mathbb{R}^D \rightarrow \mathbb{R}$ for $\mathbf{x} = [x \ y]^T$ by

$$\ell_a(\mathbf{x}) = \mathbb{1}_{\{x \notin [x_{\min}^{(a)}, x_{\max}^{(a)}]\}} \min_{x' \in \{x_{\min}^{(a)}, x_{\max}^{(a)}\}} |x' - x|^2 + \mathbb{1}_{\{y \notin [y_{\min}^{(a)}, y_{\max}^{(a)}]\}} \min_{y' \in \{y_{\min}^{(a)}, y_{\max}^{(a)}\}} |y' - y|^2. \quad (9)$$

Intuitively, $\ell_a(\mathbf{x})$ penalizes positions that are outside of the LoS bounding box $\mathcal{B}^{(a)}$: If \mathbf{x} is in the LoS bounding box $\mathcal{B}^{(a)}$, then $\ell_a(\mathbf{x})$ is equal to zero; otherwise, the loss $\ell_a(\mathbf{x})$ is equal to the minimum squared-distance to $\mathcal{B}^{(a)}$. One can now train a neural network that implements the channel charting function g_{θ} by minimizing the loss \mathcal{L}_{box} ; this approach is weakly supervised as the loss incorporates partial information on the ground-truth labels (i.e., each AP’s LoS bounding box).

We conclude by noting that a loss based on bounding boxes of zones was also proposed in [34]; however, this approach required zone-labeled CSI samples. In contrast, we deduce our bounding boxes solely based on the AP-side receive powers, without requiring any explicit CSI labels.

C. Combining all Loss Functions

We propose to combine the three loss functions \mathcal{L}_{t} , \mathcal{L}_{bi} and \mathcal{L}_{box} , since \mathcal{L}_{t} helps to preserve local neighborhood relations whereas \mathcal{L}_{bi} and \mathcal{L}_{box} help to anchor the channel chart in real-world coordinates; moreover, false triplets in \mathcal{L}_{t} and false AP pairs in \mathcal{L}_{bi} can be counterbalanced. We define the resulting multi-loss as follows:

$$\mathcal{L}_{\text{m}} = \lambda_{\text{t}} \mathcal{L}_{\text{t}} + \lambda_{\text{bi}} \mathcal{L}_{\text{bi}} + \lambda_{\text{box}} \mathcal{L}_{\text{box}}. \quad (10)$$

Here, λ_{t} , λ_{bi} , and λ_{box} are nonnegative regularization parameters that individually weight the losses; the choice of these parameters is briefly discussed in Sec. IV-A.

One can train a neural network that implements the channel charting function g_θ by minimizing the loss \mathcal{L}_m ; this approach is a hybrid between self- and weakly-supervised learning due to the reasons mentioned in Sec. II-E, Sec. III-A, and Sec. III-B.

IV. METHODS, BASELINES, AND PERFORMANCE METRICS

We now briefly outline the neural network architecture used for learning the channel charting function. We then detail the proposed methods and baselines, and we introduce the performance metrics used in our evaluation.

A. Learning the Channel Charting Function

We use a six-layer fully connected neural network for the channel charting (and positioning) functions g_θ . With input feature dimension D' , the neural network has $\{D', D'/2, D'/4, D'/8, D'/16, D\}$ activations per layer, and we set the output dimension to $D = 2$ since the height of the UE is fixed. All layers except for the last one use ReLU activations, whereas the last layer uses a linear activation function. We employ Glorot initialization [44] for the last layer, and He initialization [45] for the remaining layers. We use the Adam optimizer during training.

The hyperparameters used in the loss functions for training, namely T_c and M_t in the triplet loss from (4), M_b in the bilateration loss from (7), and the regularization parameters in the combined loss (λ_t , λ_{bi} , and λ_{box}) from (10) affect the global scale of the resulting channel charts. Unless stated otherwise, we keep $\lambda_t = 1$ and adjust the remaining hyperparameters. We assume that the training dataset includes CSI from the entire area of interest in which the UEs are moving, and we choose these hyperparameters heuristically so that the resulting channel charts approximately match the size and shape of the area of interest.

B. Proposed Methods and Baselines

All of our proposed methods and baselines use the same neural network architecture (cf. Sec. IV-A) but are trained with different loss functions, which we detail next.

Proposed 1 (P1): For our first proposed method, we extract the receive power for each UE position and each AP as described in Sec. III. We train the neural network using the summation³ of \mathcal{L}_{bi} and \mathcal{L}_{box} defined in (7) and (8), respectively; in other words, we use \mathcal{L}_m defined in (10) with $\lambda_t = 0$ and $\lambda_{bi}, \lambda_{box} > 0$. Here, we aim to demonstrate the efficacy of only the bilateration and LoS bounding-box losses. We reiterate that, due to the reasons mentioned in Sec. III-A and Sec. III-B, this approach is weakly-supervised.

Proposed 2 (P2): For our second proposed method, we assume that timestamps are available for all CSI features in the training set; we also extract the receive power for each UE position at each AP as described in Sec. III. We train the neural network using the multi-loss \mathcal{L}_m combining triplet, bilateration, and LoS bounding-box losses defined in (10)

³For LoS bounding-box loss, we only used the LoS bounding box of the AP with the largest power since we did not observe any improvement from using all APs in $\hat{\mathcal{A}}$ in our experiments.

with $\lambda_t, \lambda_{bi}, \lambda_{box} > 0$. We reiterate that due to the reasons mentioned in Sec. III-C regarding each component of the loss, this approach is a hybrid between self- and weakly-supervised learning.

Baseline 1 (B1): For this baseline, we assume that the timestamps are available for all CSI features in the training set. We train the neural network using only the triplet loss \mathcal{L}_t defined in (4). Our aim in presenting this baseline is to compare the performance of our methods to (purely) self-supervised channel charting. We reiterate that this approach is self-supervised due to the reasons mentioned in Sec. II-E. Note that the resulting channel charts are often of high quality but embedded in arbitrary coordinates.

Baseline 2 (B2): For this baseline, we assume that, while timestamps are available for all CSI features in the training set, ground-truth UE positions are available for a subset \mathcal{S} of the training set. We first learn a channel charting function g_θ in a self-supervised manner in the same way as baseline B1; then, we estimate an affine transform that maps the output of g_θ to real-world coordinates as in [37], [38], [40]

$$\{\hat{\mathbf{A}}, \hat{\mathbf{b}}\} = \arg \min_{\mathbf{A} \in \mathbb{R}^{D \times D}, \mathbf{b} \in \mathbb{R}^D} \sum_{n \in \mathcal{S}} \|(\mathbf{A}g_\theta(\mathbf{f}^{(n)}) + \mathbf{b}) - \tilde{\mathbf{x}}^{(n)}\|^2, \quad (11)$$

where we solve a least-squares problem to minimize the error between the affine-transformed channel chart positions and known ground-truth positions. Finally, we apply the estimated affine transform to the channel-chart pseudo-positions as $\hat{\mathbf{x}}^{(n)} = \hat{\mathbf{A}}g_\theta(\mathbf{f}^{(n)}) + \hat{\mathbf{b}}$. Our aim in presenting this baseline is to (i) showcase whether the channel charts can always be mapped to real-world coordinates through merely an affine transform, and (ii) compare the performance of our proposed method of incorporating the real-world coordinates directly into the channel charting function (without using ground-truth positions) to the two-stage approach of mapping a channel chart to real-world coordinates (using ground-truth positions). We reiterate that estimating the affine transform here relies on known ground-truth positions.

Baseline 3 (B3): For this baseline, we assume that, while the timestamps are available for all samples in the training set, ground-truth labels are available for a small subset \mathcal{S} of the training set. Hence, we can define a mean-squared error (MSE) loss for the labeled samples as follows:

$$\mathcal{L}_{\widehat{\text{MSE}}} = \frac{1}{|\mathcal{S}|} \sum_{n \in \mathcal{S}} \|g_\theta(\mathbf{f}^{(n)}) - \tilde{\mathbf{x}}^{(n)}\|^2. \quad (12)$$

We train the neural network using the combined triplet and MSE loss function defined as

$$\mathcal{L}_{t, \widehat{\text{MSE}}} = \mathcal{L}_t + \mathcal{L}_{\widehat{\text{MSE}}}. \quad (13)$$

Since the loss $\mathcal{L}_{t, \widehat{\text{MSE}}}$ utilizes a subset of the ground-truth UE positions in addition to the triplet loss, this baseline is semi-supervised. Our aim in presenting this baseline is to compare the performance of our methods to semi-supervised positioning techniques (e.g., [29]–[34]), and showcase whether our approach can achieve comparable performance to semi-supervised techniques without using any ground-truth UE position information.

Baseline 4 (B4): For this baseline, we assume that ground truth positions are available for all samples in the training set. We train the neural network with the MSE loss for all training samples. We denote the loss here by \mathcal{L}_{MSE} to distinguish it from the loss over a subset of the training samples as in baseline B3. Since the loss \mathcal{L}_{MSE} requires ground-truth labels for *all* training samples, this approach is fully supervised. Our aim in presenting this baseline is to compare the performance of our methods to fingerprinting methods that process CSI features with neural networks (see, e.g., [23], [25] and the references therein). This baseline is also an indicator for the best-possible positioning performance achievable with the neural network architecture described in Sec. IV-A.

C. Performance Metrics

We evaluate the performance of the proposed methods and baselines using six metrics. The first four metrics measure the quality of the channel chart; we refer to [46] for the details. The latter two metrics measure positioning accuracy.

Trustworthiness (TW): This penalizes neighborhood relationships in latent space that are not present in the real-world positions [47]; TW values are in $[0, 1]$ with optimal value 1.

Continuity (CT): This measures how well neighborhood relationships between the real-world positions are preserved in latent space [47]; CT values are in $[0, 1]$ with optimal value 1.

Kruskal stress (KS): This measures the dissimilarity between pairwise distances in the real-world positions and pairwise distances in latent space [48]; KS values are in $[0, 1]$ with optimal value 0.

Rajski distance (RD): This measures the difference between the mutual information and joint entropy of the distribution of pairwise distances in the real-world positions and latent space [49]; RD values are in $[0, 1]$ with optimal value 0.

Mean distance error: This measures the average error in the UE position estimates in Euclidean norm over all UE positions; this metric is nonnegative with optimal value 0.

95th percentile distance error: This measures the 95th percentile of the error in the UE position estimates in Euclidean norm over all UE positions; this metric is nonnegative with optimal value 0.

V. RESULTS

We assess the performance of our proposed methods and the considered baselines using three distinct CSI datasets obtained from different scenarios: a simulated outdoor scenario, a simulated indoor scenario, and a measurement-based indoor scenario. In the subsections below, we describe each scenario, provide a brief analysis of the AP-side receive power, and show the ground-truth position, channel chart, and estimated position plots, followed by assessing the performance metrics from Sec. IV-C for the proposed methods and baselines.

In the simulated scenarios, we add noise to the truncated channel matrices so that the highest SNR per AP is 25 dB. In all three scenarios, we use 80% of the dataset for training and 20% for testing. For baselines B2 and B3, we select the subset of ground-truth labeled CSI samples uniformly at random from

the training set. All plots and performance metrics are based on the test set.

In Figs. 2, 5, and 7, we visually compare the ground-truth positions as well as channel charts in arbitrary and real-world coordinates for each scenario; in Tbls. II, III, and IV, we provide the respective performance metrics. The performance metrics reflect the average based on 10 random initializations of the neural network parameters. For the positioning metrics, we also report the standard deviation; we omitted this step for the latent space quality metrics since these metrics are all between $[0, 1]$ which results in small standard deviations.

Since B1 produces channel charts in arbitrary coordinates, we omit the two distance error metrics for baseline B1 in the performance metric tables. Moreover, to prevent redundancy, we exclude the figures depicting estimated positions for supervised learning baseline B4, as these figures closely resemble those of the ground-truth positions.

A. Simulated Outdoor Scenario

1) Description: For our first scenario, we consider a D-MIMO urban environment in which multiple APs are distributed around a rectangular area of size $83\text{ m} \times 122\text{ m}$, while the UE traverses a trajectory to cover this region with north-south and east-west meandering; see Fig. 3 (a) for a snapshot of the simulation environment, and Fig. 2 (a) for an illustration of the UE and AP positions along with the LoS bounding box used for all APs. We simulate a sub-6-GHz scenario with channel vectors from Remcom's Wireless InSite ray-tracing software [13]. The first column of Tbl. I summarizes the simulation parameters.⁴ Each CSI matrix $\mathbf{H}^{(n)}$, $n \in \mathcal{N}$ is of dimension 24×1200 ; each CSI feature vector is of dimension $D' = 24 \times 8 = 192$, where we use the $C = 8$ first taps and the feature extraction pipeline outlined in Sec. II-C.

2) Analysis of AP-Side Receive Power: In this scenario, we know that all APs have a LoS path to all UE positions; therefore, we can set $P_{\text{thr}} = -\infty$ to include all APs in $\tilde{\mathcal{A}}^{(n)}$ from (5). We exemplify the power-distance relation exploited by bilateration loss in Fig. 1. Here, we show the receive power at one AP depending on the distance to the UE in the xy-plane; we ignore the distance in the z-axis since the heights are fixed. We remark that our proposed methods do not use ground-truth positions, and thus, are uninformed of the UE's distance to APs; we do not make any decisions based on the power-distance plot and we merely provide this plot as a proof-of-concept. Evidently, the power generally decreases with distance, but small-scale fading causes the power to fluctuate quite substantially among the different UE positions which are at approximately the same distance to the AP. Furthermore, the received power increases⁵ with distance until about 10 m, which negatively affects approaches that rely on the power being the highest near the AP, e.g., the method in [37].

⁴This simulation scenario is slightly different from what we presented in our conference paper [1]: In [1], we used a rectangular grid for the UE positions and eight APs; here, we used the trajectory feature of Remcom's Wireless In-Site for the UE positions and six APs for a more challenging scenario.

⁵This behavior can be attributed to the antenna radiation pattern, which causes the receive power to reduce if a UE approaches the area below an AP.

TABLE I
PARAMETERS FOR EACH CONSIDERED SCENARIO

Parameter	Value or type of parameter for each scenario		
	Simulated outdoor	Simulated indoor	Measured indoor [2]
Number of APs	$A = 6$	$A = 8$	$A = 4$
Number of antennas per AP	$M_R = 4$	$M_R = 4$	$M_R = 8$
APs' antenna array structure	Uniform linear array	Uniform linear array	Uniform rectangular array, 2×4
Number of UE positions	14 642	14 606	16 778
Spacing between UE positions	40 cm	2.5 cm	(not fixed)
AP antenna height	10 m	2 m	1.56 – 1.78 m
AP antenna spacing	Half-wavelength	Half-wavelength	Half-wavelength
UE antenna height	1.5 m	1.5 m	≈ 0.94 m
AP and UE antenna type	Omnidirectional	Omnidirectional	Omnidirectional
Carrier frequency	1.9 GHz	2.4 GHz	1.272 GHz
Bandwidth	20 MHz	20 MHz	50 MHz
Number of used subcarriers	$W = 1200$	$W = 52$	$W = 1024$
Maximum SNR per AP	25 dB	25 dB	–

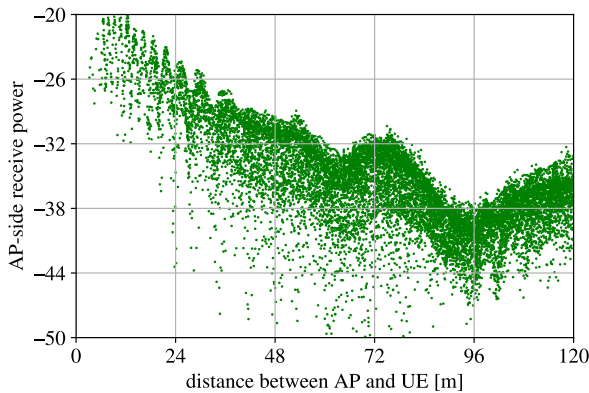


Fig. 1. Receive power (in decibels) at one AP for the simulated outdoor scenario with respect to the AP-to-UE distance in the xy-plane.

Since a smaller difference in power is more likely to be caused by small-scale fading (and not by distance), we would be less confident in deducing which AP might be closer. Hence, observing that the AP-side receive power is not perfectly inversely proportional to distance motivates the margin parameter M_p in (6). By setting $M_p > 0$, we can avoid some false AP pairs, i.e., pairs $(a_c, a_f) \in \mathcal{P}^{(n)}$ for which $\|\tilde{\mathbf{x}}^{(n)} - \tilde{\mathbf{x}}^{(a_c)}\| > \|\tilde{\mathbf{x}}^{(n)} - \tilde{\mathbf{x}}^{(a_f)}\|$. For this CSI dataset, margins M_p of 0, 3, and 6 result in false AP pair ratios of 16.6%, 0.06%, and 0.02% for all UEs, while the average number of AP pairs in the set $\mathcal{P}^{(n)}$ given by $\frac{1}{N} \sum_{n=1}^N |\mathcal{P}^{(n)}|$ is 15, 9.2, and 4.63, respectively. Clearly, there exists a trade-off in choosing M_p : Increasing M_p leads to fewer *false* AP pairs at the cost of fewer AP pairs in $\mathcal{P}^{(n)}$ from (6), which yields more accurate but fewer reference points for weakly-supervised learning (and vice versa).

3) *Parameter Settings*: For our proposed method P1, we set $M_t = M_b = 10$, $M_p = 3$, $\lambda_t = 0$, and $\lambda_{bi} = \lambda_{box} = 1$. Since there is no blockage in the area of interest, i.e., the UEs should have a LoS path to all APs, we set $P_{thr} = -\infty$. P2 shares the same parameters as P1 except for the triplet loss, for which we use $\lambda_t = 1$, $T_c = 10$, and $M_t = 10$. B1, B2, and B3 share the same triplet loss parameters as P2.

For the baselines B2 and B3, we used the ground-truth

positions of 10 and 400 CSI samples, respectively. With B2, we demonstrate the performance of learning an affine transform from a handful of labeled samples. With B3, we demonstrate approximately how many ground-truth labeled samples are required to achieve comparable performance to P2.

4) *Performance Evaluation*: In Fig. 2, we observe that all methods result in an almost rectangular chart preserving the color gradient and resembling the ground-truth positions, as desired. Potentially due to the shape of the area and the trajectory of the UE, the self-supervised baseline B1 performs surprisingly well in terms of the global geometry; the channel chart only needs to be rotated, which is exactly what B2 yields.

In Tbl. II, we observe that affine transform-based B2 has the best performance in all metrics, even outperforming the supervised baseline B4. The reason behind the performance of B2 is that the self-supervised baseline B1 luckily already represents both the local and global geometry very well, as confirmed by the large values of TW and CT, and small values of KS and RD, respectively. Hence, we note that *when* the channel chart represents the global geometry well, then an affine transform learned from a handful of labeled samples can result in a good positioning performance.⁶ However, the shortcomings of B2 will be apparent in our next scenario. While the channel chart of P1 demonstrates that the bilateration and LoS bounding-box losses alone can help create a channel chart in real-world coordinates, P1 is outperformed by all the other methods in all performance metrics. P2 outperforms the semi-supervised baseline B3 in the latent space quality metrics. P2 is slightly better than B3, by approximately 0.3m in mean and 2 m in the 95th percentile, while holding the advantage of not requiring any ground-truth positions. P2 has a higher positioning error than B2 by approximately 5 m in mean and 11 m in the 95th percentile.

We reiterate that the proposed method P2 does not require any ground-truth UE position information as opposed to baselines B2, B3, and B4. It is remarkable that B3 would require *at least* 400 ground-truth labeled samples to achieve the same performance as P2. These results demonstrate the

⁶Here, we have observed no significant improvement from further increasing the number of labeled samples.

efficacy of our proposed method P2 in a large, outdoor area with LoS channels.

B. Simulated Indoor Scenario

1) *Description*: For our second scenario, we consider a challenging indoor environment where many APs are in non-LoS for a given UE position. At least one AP is in the LoS of the UE while the UE traverses a trajectory to cover each hallway and room; see Fig. 3(b) for a snapshot of the simulation environment, and see Fig. 5(a) for an illustration of the UE and AP positions along with three APs' LoS bounding boxes as examples; here, we omit to show the LoS bounding boxes of the remaining five APs to avoid crowding the figure. We simulate a sub-6-GHz scenario with channel vectors from Remcom's Wireless InSite ray-tracing software [13]. The second column of Tbl. I summarizes the simulation parameters. Each CSI matrix $\mathbf{H}^{(n)}$, $n \in \mathcal{N}$, is of dimension 32×52 ; each CSI feature vector is of dimension $D' = 32 \times 8 = 256$, where we use the $C = 8$ first taps and the feature extraction pipeline from Sec. II-C.

2) *Analysis of AP-Side Receive Power*: In this scenario, we know that the UE does not have a LoS path to some APs at each position; therefore, we need to choose a power threshold to estimate the LoS APs in $\tilde{\mathcal{A}}^{(n)}$ from (5). We choose this threshold based on the AP-side receive power $P^{(n,a)}$ over time t_n , as exemplified for one of the APs in Fig. 4(a). Here, we observe a steep drop in the power at around -30 dB, and set $P_{\text{thr}} = -30$. We omit an ablation study that shows P_{thr} is robust to small deviations for brevity. We now exemplify the power-distance relation exploited by our bilateration loss in (7) and the impact of P_{thr} for the same AP as Fig. 4(a) in Fig. 4(b). Here, we clearly observe the need for choosing an appropriate power threshold P_{thr} as many UE positions are close to the AP while the AP-side receive power is low; we should not use this AP in bilateration loss for such UE positions. As desired, we observe that the receive power indeed falls below our chosen power threshold P_{thr} for these positions. Moreover, the UE positions where the AP-side receive power is higher than P_{thr} follow the same trend as Fig. 1, i.e., the power generally decreases with distance. Therefore, we conclude that our choice of P_{thr} is suitable for classifying the LoS APs to be used in bilateration and LoS bounding-box losses.

For this CSI dataset, a threshold $P_{\text{thr}} = -30$ with margins M_p of 0, 3, and 6 result in false AP-pair ratios of 15.5%, 3.4%, and 0.2% for all UEs, while the average number of AP pairs in the set $\mathcal{P}^{(n)}$ given by $\frac{1}{N} \sum_{n=1}^N |\mathcal{P}^{(n)}|$ is 1.03, 0.60, and 0.30, respectively. Once again, we observe the trade-off in choosing M_p : Increasing M_p leads to fewer false AP pairs at the cost of fewer AP pairs in $\mathcal{P}^{(n)}$ from (6).

3) *Parameter Settings*: For our proposed method P1, we set $M_t = M_b = 1$, $M_p = 3$, $\lambda_t = 0$, $\lambda_{\text{bi}} = \lambda_{\text{box}} = 1$, and $P_{\text{thr}} = -30$. P2 shares the same parameters as P1 except for the triplet loss, for which we use $\lambda_t = 1$, $T_c = 2$, and $M_t = 1$. B1, B2, and B3 share the same triplet loss parameters as P2.

For the baselines B2 and B3, we used the ground-truth positions of 10 000 and 50 CSI samples, respectively. With B2, we demonstrate that the affine transform fails to yield a good

representation of real-world coordinates no matter how many ground-truth positions were used. With B3, we demonstrate approximately how many ground-truth labeled samples are required to achieve comparable performance to P2.

4) *Performance Evaluation*: In Fig. 5, we observe that P1, P2, and B3 all yield similar results while the quality of P1 is (unsurprisingly) slightly worse. However, even in P1, we observe that the UE positions are mostly in the correct zones (i.e., rooms and hallways), which demonstrates the capabilities of the bilateration and LoS bounding-box losses in D-MIMO scenarios with many APs. Moreover, we observe that B2 is highly inaccurate, as we could not correct for the distortion in B1 through an affine transform no matter how many ground-truth labels we use to find such a transform. This example demonstrates that channel charts may have non-affine distortions; hence, mapping channel charts to real-world coordinates through an affine transform is not a generally applicable method.

In Tbl. III, we observe—as expected—that B4 achieves the best performance in all metrics. P2 has approximately the same performance as the semi-supervised baseline B3 in the latent space quality metrics. P2 has a slightly higher positioning error than B3, by approximately 0.1 m in mean and 0.3 m in the 95th percentile. P2 has a higher positioning error than B4 by approximately 0.5 m in mean and 1.3 m in the 95th percentile. This result demonstrates the efficacy of our proposed method P2 in an indoor area with many non-LoS paths.

C. Measurement-Based Indoor Scenario

1) *Description*: For our third scenario, we utilize the measured channel vectors from the DICHASUS datasets [2], [50]. The third column of Tbl. I summarizes the measurement parameters. These measurements are from a D-MIMO communication system in a factory environment, where the transmitter is a robot moving in various trajectories in an L-shaped area. The inner corner of this L-shaped area has a large metal container potentially blocking the LoS path to some APs, while every position in the measurement area has a LoS path to at least one AP; see Fig. 7(a) for an illustration of the UE and AP positions along with the two LoS bounding boxes used for the top and bottom pairs of APs. We use the CSI from the first three trajectories of the dataset in [2] and take every fourth sample to reduce the total dataset size. We apply a rotation of 12° to all positions in order to simplify setting the rectangular LoS bounding boxes of APs. Each CSI matrix $\mathbf{H}^{(n)}$, $n \in \mathcal{N}$ is of dimension 32×1024 ; each CSI feature vector is of dimension $D' = 32 \times 13 = 416$, where we use the $C = 13$ taps described in [40] and the feature extraction pipeline from Sec. II-C.

2) *Analysis of AP-Side Receive Power*: In this scenario, we know that not all UE positions have a LoS path to all APs; therefore, we first need to choose a power threshold to estimate the LoS APs to be used in bilateration and LoS bounding-box losses. We choose this threshold based on the AP-side receive power $P^{(n,a)}$ over time t_n , as exemplified for one of the APs in Fig. 6(a). Here, we observe a steep drop in the power at around 15 dB, and set $P_{\text{thr}} = 15$. For brevity, we omit an

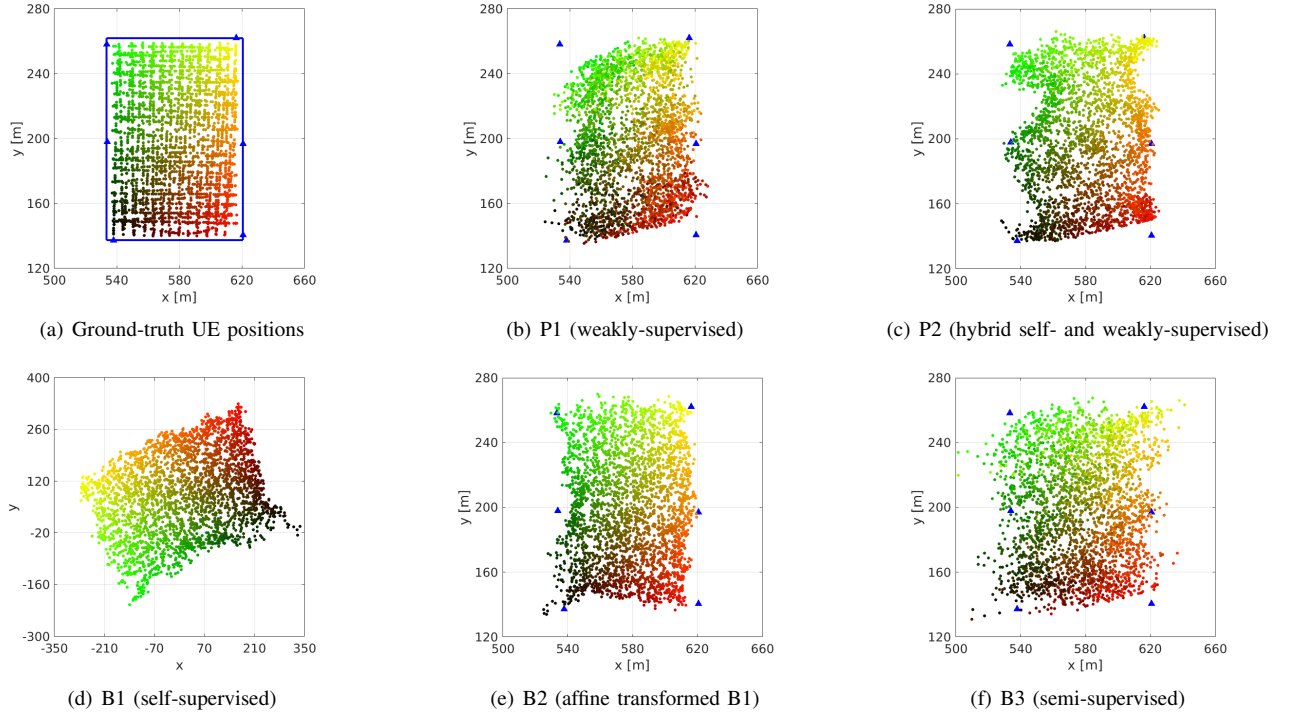


Fig. 2. Results for the simulated outdoor scenario: (a) ground-truth UE positions (green-to-red gradient colored area), AP positions (blue triangles), and the LoS bounding box of all APs; and (b-f) the channel charts or positioning estimates for the proposed (P) and baseline (B) methods. Since the output of baseline B2 is in arbitrary coordinates, the AP positions are not shown in (d). The proposed method P2 achieves comparable results in real-world coordinates as the semi-supervised baseline B3 but without requiring known UE positions during training.

TABLE II
CHANNEL CHARTING AND POSITIONING PERFORMANCE COMPARISON FOR THE SIMULATED OUTDOOR SCENARIO

Method	Figure	Latent space quality metrics				Positioning error [m]	
		TW \uparrow	CT \uparrow	KS \downarrow	RD \downarrow	Mean \downarrow	95th percentile \downarrow
P1	2 (b)	0.923	0.922	0.238	0.864	14.18 ± 0.62	29.98 ± 1.306
P2	2 (c)	0.984	0.985	0.123	0.710	8.75 ± 0.31	17.85 ± 0.66
B1	2 (d)	0.998	0.998	0.068	0.550	–	–
B2	2 (e)	0.998	0.998	0.064	0.533	3.15 ± 0.34	7.06 ± 0.99
B3	2 (f)	0.964	0.962	0.166	0.775	9.07 ± 0.47	20.76 ± 1.28
B4	–	0.994	0.994	0.069	0.563	3.57 ± 0.18	7.34 ± 0.37

TABLE III
CHANNEL CHARTING AND POSITIONING PERFORMANCE COMPARISON FOR THE SIMULATED INDOOR SCENARIO

Method	Figure	Latent space quality metrics				Positioning error [m]	
		TW \uparrow	CT \uparrow	KS \downarrow	RD \downarrow	Mean \downarrow	95th percentile \downarrow
P1	5 (b)	0.950	0.952	0.195	0.791	1.61 ± 0.03	3.32 ± 0.12
P2	5 (c)	0.979	0.976	0.144	0.710	1.15 ± 0.04	2.84 ± 0.44
B1	5 (d)	0.983	0.968	0.347	0.857	–	–
B2	5 (e)	0.967	0.955	0.373	0.883	3.21 ± 0.54	6.66 ± 0.90
B3	5 (f)	0.970	0.974	0.184	0.753	1.31 ± 0.18	3.53 ± 1.46
B4	–	0.988	0.989	0.082	0.572	0.63 ± 0.01	1.55 ± 0.02

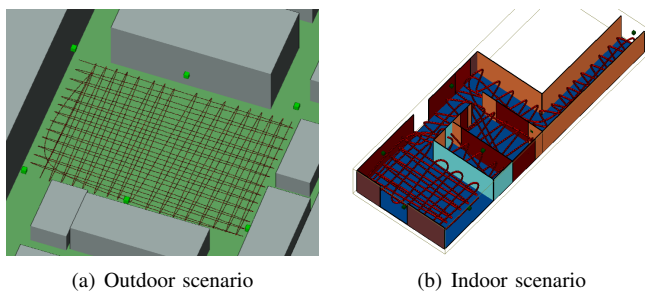
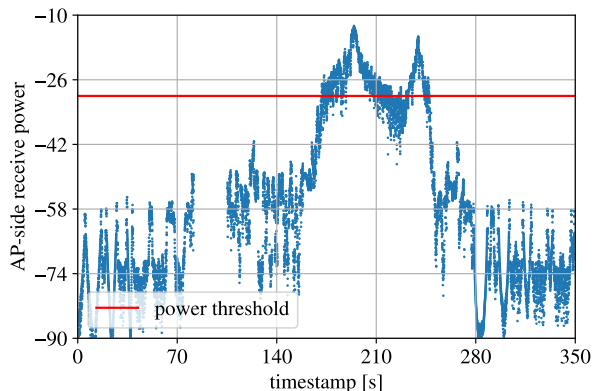
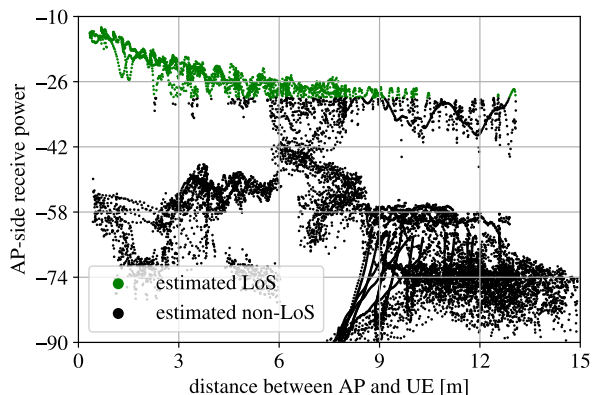


Fig. 3. Simulated D-MIMO scenarios: (a) outdoor scenario with 14642 UE positions and $A = 6$ APs; (b) indoor scenario with 14606 UE positions and $A = 8$ APs. Each AP (green boxes) is equipped with $M_R = 4$ antennas.



(a) AP-side receive power with respect to time



(b) AP-side receive power versus AP-to-UE distance

Fig. 4. Receive power (in decibels) at one AP for the simulated indoor scenario with respect to (a) timestamps and (b) AP-to-UE distance in the xy-plane. In (a), the red line designates the power threshold chosen to identify LoS APs. In (b), the power values above the threshold (highlighted with green) indicate instances where the AP is estimated to be in LoS.

ablation study that shows P_{thr} is robust to small deviations. We now exemplify the power-distance relation exploited by our bilateration loss in (7) and the impact of P_{thr} for the same AP as Fig. 6(a) in Fig. 6(b). Here, we observe the urgent need for choosing an appropriate power threshold P_{thr} as there are many UE positions that are close to the AP while the AP-side receive power is low; we should not use this AP in bilateration loss for such UE positions. As desired, we observe that the receive power indeed falls below our chosen power threshold P_{thr} for these positions. Moreover, the UE positions for which

the AP-side receive power is higher than P_{thr} follow the same trend as Fig. 1, i.e., the power generally decreases with distance. Therefore, we conclude that our choice of P_{thr} is suitable for classifying the LoS APs to be used in bilateration and LoS bounding-box losses.

For this CSI dataset, margins M_p of 0, 3, and 6 result in false AP pair ratios of 27.5%, 5%, and 1.8% for all UEs, while the average number of AP pairs in the set $\mathcal{P}^{(n)}$ given by $\frac{1}{N} \sum_{n=1}^N |\mathcal{P}^{(n)}|$ is 1.7, 0.44, and 0.10, respectively. Once again, we observe the trade-off in choosing M_p : Increasing M_p leads to fewer false AP pairs at the cost of fewer AP pairs in $\mathcal{P}^{(n)}$ from (6).

3) *Parameter Settings*: For our proposed method P1, we set $M_t = M_b = 0.5$, $M_p = 3$, $\lambda_t = 0$, and $\lambda_{\text{bi}} = \lambda_{\text{box}} = 1$. P2 shares the same parameters as P1 except for the triplet loss, where we use $\lambda_t = 1$, $T_c = 5$, and $M_t = 0.5$. B1, B2, and B3 use the same triplet loss parameters as P2.

For the baselines B2 and B3, we used the ground-truth positions of 10 and 30 CSI samples, respectively. With B2, we demonstrate the performance of learning an affine transform from a small number of labeled samples. With B3, we demonstrate how many ground-truth labeled samples one would approximately need to achieve comparable performance to that of P2.

4) *Performance Evaluation*: In Fig. 7, we observe that all methods that utilize triplet loss (i.e., P2, B1, B2, and B3) separate the red and green regions of the positions in an L-shaped chart resembling the ground-truth positions. However, for P1, the limitation of using bilateration and LoS bounding-box loss without the triplet loss is clear: With few APs and relatively large bounding boxes, the channel chart cannot reflect the UE positions well.

In Tbl. IV, we observe, as expected, that B4 achieves the best performance in all metrics. B2 is the second-best in all metrics as we again observe the advantage of starting from a “good” channel chart for the affine transform-based approach. P2 has a better performance in TW and CT, and a slightly worse performance in KS and RD than B3. P2 has a higher positioning error than B4 by approximately 1.2 m in mean and 2.6 m in the 95th percentile. P2 has a slightly higher positioning error than B2, by approximately 0.5 m in mean and 1.3 m in the 95th percentile; these differences are smaller for B3. This result demonstrates the efficacy of our proposed method P2 for measured channels in an industrial environment, with few APs and many non-LoS paths.

VI. CONCLUSIONS AND FUTURE WORK

We have proposed the bilateration loss and LoS bounding-box loss which enable weakly-supervised channel charting in real-world coordinates, without requiring geometric models, accurate AP synchronization, or ground-truth UE positions. The bilateration loss utilizes the known AP positions in a D-MIMO scenario by comparing the received power at pairs of APs that are estimated to have a LoS path to the UE and places the UE closer to the AP which receives higher power. The LoS bounding-box loss places the UE in the bounding box of each AP that is estimated to have a LoS path. We have

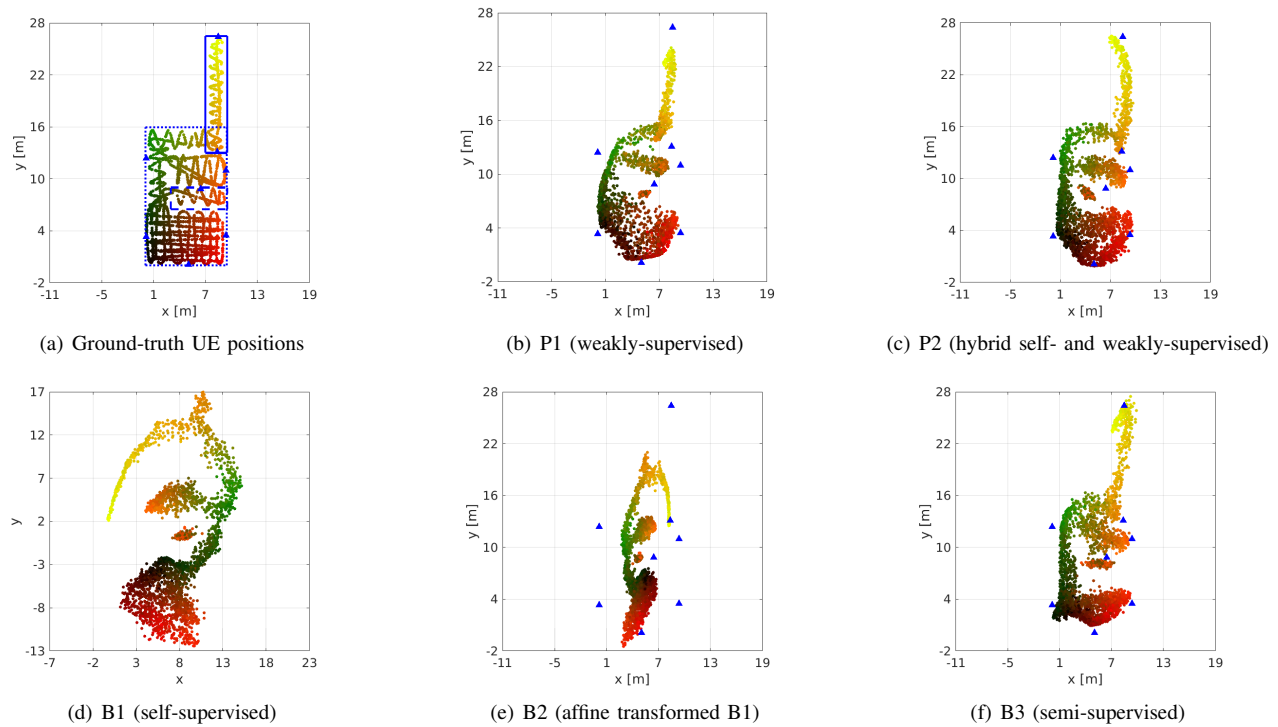


Fig. 5. Results for the simulated indoor scenario: (a) ground-truth UE positions (green-to-red gradient colored area), AP positions (blue triangles), and the LoS bounding box of three APs (blue solid and dashed lines); and (b-f) the channel charts or positioning estimates for the proposed (P) and baseline (B) methods. Since the output of baseline B2 is in arbitrary coordinates, the AP positions are not shown in (d). The proposed method P2 achieves comparable results in real-world coordinates as the semi-supervised baseline B3 but without requiring known UE positions during training.

TABLE IV
CHANNEL CHARTING AND POSITIONING PERFORMANCE COMPARISON FOR THE MEASURED INDOOR SCENARIO

Method	Figure	Latent space quality metrics				Positioning error [m]	
		TW \uparrow	CT \uparrow	KS \downarrow	RD \downarrow	Mean \downarrow	95th percentile \downarrow
P1	7 (b)	0.842	0.852	0.441	0.961	2.83 ± 0.24	6.28 ± 0.61
P2	7 (c)	0.972	0.980	0.192	0.799	1.33 ± 0.03	3.05 ± 0.17
B1	7 (d)	0.989	0.990	0.179	0.769	–	–
B2	7 (e)	0.990	0.991	0.125	0.678	0.83 ± 0.37	1.78 ± 0.76
B3	7 (f)	0.955	0.969	0.182	0.783	1.02 ± 0.06	2.47 ± 0.30
B4	–	0.998	0.998	0.036	0.401	0.18 ± 0.01	0.42 ± 0.02

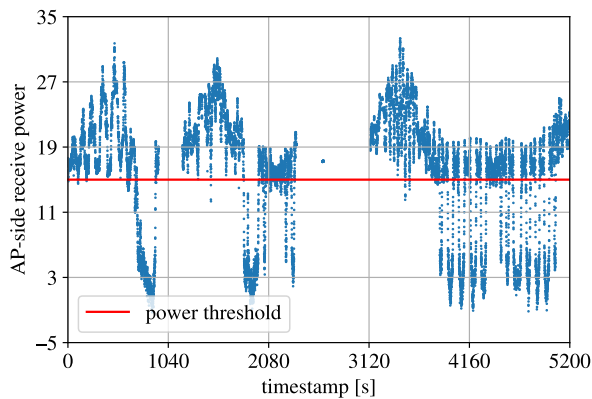
demonstrated that a multi-loss combining the bilateration and LoS bounding-box losses with the triplet loss from [12] is sufficient to generate high-quality channel charts in real-world coordinates using three different datasets: two datasets based on a commercial ray tracer (one indoors and one outdoors) and one based on indoor channel measurements. We have shown through a comparison with several baselines that our proposed approach can achieve the performance of using a subset of ground-truth labeled CSI samples, which has the advantage that no ground-truth positions need to be acquired. In addition, the size of the subset of known CSI samples for semi-supervised baseline methods depends heavily on the scenario and the size of the area of interest. Moreover, we have demonstrated that a two-stage approach that maps a learned channel chart to real-world coordinates using an affine transform may completely fail depending on the channel chart quality.

There are many avenues for future work. To improve positioning accuracy, the bounding boxes could be extended

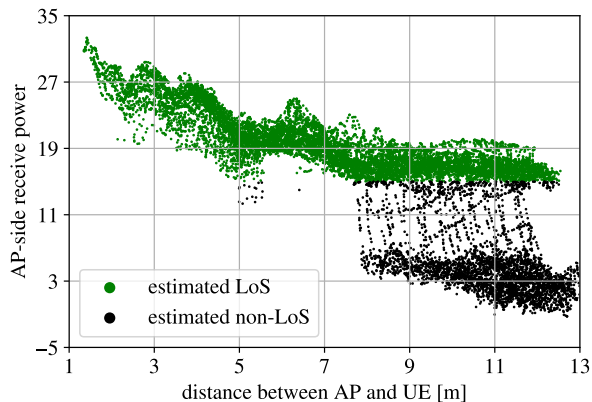
to more general shapes for improved accuracy and new loss functions that compare AP angle-of-arrival information besides receive power could be utilized as well. In addition, investigating the efficacy of other dissimilarity metrics further to improve the quality of the learned channel charts is part of ongoing work.

REFERENCES

- [1] S. Taner, V. Palhares, and C. Studer, “Channel charting in real-world coordinates,” in *Proc. IEEE Global Telecommun. Conf. (GLOBECOM)*, Dec. 2023, pp. 3940–3946.
- [2] F. Euchner and M. Gauger, “CSI Dataset dichasus-cf0x: Distributed Antenna Setup in Industrial Environment, Day 1,” 2022. [Online]. Available: <https://doi.org/doi:10.18419/darus-2854>
- [3] C. Studer, S. Medjkouh, E. Gönültaş, T. Goldstein, and O. Tirkkonen, “Channel charting: Locating users within the radio environment using channel state information,” *IEEE Access*, vol. 6, pp. 47 682–47 698, Aug. 2018.
- [4] L. Ribeiro, M. Leinonen, H. Al-Tous, O. Tirkkonen, and M. Juntti, “Channel charting aided pilot reuse for massive MIMO systems with spatially correlated channels,” *IEEE Open J. Commun. Soc.*, vol. 3, pp. 2390–2406, Dec. 2022.



(a) AP-side receive power with respect to time



(b) AP-side receive power versus AP-to-UE distance

Fig. 6. Receive power (in decibels) at one AP for the measurement-based indoor scenario [2] with respect to (a) timestamps and (b) AP-to-UE distance in the xy-plane. In (a), the red line designates the power threshold chosen to identify LoS APs. In (b), the power values above the threshold (highlighted with green) indicate instances where the AP is estimated to be in LoS.

- [5] L. L. Magoarou, T. Yassine, S. Paquelet, and M. Crussière, "Channel charting based beamforming," in *Proc. Asilomar Conf. Signals, Syst., Comput.*, Oct. 2022, pp. 1185–1189.
- [6] P. Kazemi, H. Al-Tous, C. Studer, and O. Tirkkonen, "Channel charting assisted beam tracking," in *Proc. IEEE Veh. Technol. Conf. Spring (VTC-Spring)*, Jun. 2022, pp. 1–5.
- [7] T. Kallehauge, A. E. Kalør, P. Ramírez-Espinosa, M. Guillaud, and P. Popovski, "Delivering ultra-reliable low-latency communications via statistical radio maps," *IEEE Wireless Commun. Mag.*, vol. 30, no. 2, pp. 14–20, Apr. 2023.
- [8] P. Ferrand, M. Guillaud, C. Studer, and O. Tirkkonen, "Wireless channel charting: Theory, practice, and applications," *IEEE Commun. Mag.*, vol. 61, no. 6, pp. 124–130, Jun. 2023.
- [9] J. Deng, S. Medjkouh, N. Malm, O. Tirkkonen, and C. Studer, "Multipoint channel charting for wireless networks," in *Proc. Asilomar Conf. Signals, Syst., Comput.*, Oct. 2018, pp. 286–290.
- [10] F. Euchner, P. Stephan, M. Gauger, S. Dörner, and S. Ten Brink, "Improving triplet-based channel charting on distributed massive MIMO measurements," in *Proc. IEEE Int. Workshop Signal Process. Advances Wireless Commun. (SPAWC)*, Jul. 2022, pp. 1–5.
- [11] P. Agostini, Z. Utkovski, and S. Stańczak, "Federated learning for multipoint channel charting," in *Proc. IEEE Int. Workshop Signal Process. Advances Wireless Commun. (SPAWC)*, Jul. 2022, pp. 1–5.
- [12] P. Ferrand, A. Decurninge, L. G. Ordoñez, and M. Guillaud, "Triplet-based wireless channel charting: Architecture and experiments," *IEEE J. Sel. Areas Commun.*, vol. 39, no. 8, pp. 2361–2373, Jun. 2021.
- [13] Remcom, Inc. (2022) Wireless InSite. [Online]. Available: <https://www.remcom.com/wireless-insite-em-propagation-software/>
- [14] F. Wen, H. Wymeersch, B. Peng, W. P. Tay, H. C. So, and D. Yang, "A survey on 5G massive MIMO localization," *Digital Signal Process.*, vol. 94, pp. 21–28, Nov. 2019.
- [15] H. Liu, H. Darabi, P. Banerjee, and J. Liu, "Survey of wireless indoor positioning techniques and systems," *IEEE Trans. Syst., Man, Cybern. C. Appl. Rev.*, vol. 37, no. 6, pp. 1067–1080, Nov. 2007.
- [16] J. A. del Peral-Rosado, R. Raulefs, J. A. López-Salcedo, and G. Seco-Granados, "Survey of cellular mobile radio localization methods: From 1G to 5G," *IEEE Comm. Surveys & Tutorials*, vol. 20, no. 2, pp. 1124–1148, 2018.
- [17] W. Liu, Q. Cheng, Z. Deng, H. Chen, X. Fu, X. Zheng, S. Zheng, C. Chen, and S. Wang, "Survey on CSI-based indoor positioning systems and recent advances," in *Proc. Intl. Conf. Indoor Positioning and Indoor Navigation (IPIN)*, Sep. 2019, pp. 1–8.
- [18] E. Widdison and D. G. Long, "A review of linear multilateration techniques and applications," *IEEE Access*, vol. 12, pp. 26 251–26 266, Feb. 2024.
- [19] S. He and S.-H. G. Chan, "Wi-Fi fingerprint-based indoor positioning: Recent advances and comparisons," *IEEE Comm. Surveys & Tutorials*, vol. 18, no. 1, pp. 466–490, 2016.
- [20] X. Wang, L. Gao, S. Mao, and S. Pandey, "CSI-based fingerprinting for indoor localization: A deep learning approach," *IEEE Trans. Veh. Technol.*, vol. 66, no. 1, pp. 763–776, Jan. 2017.
- [21] J. Vieira, E. Leitingner, M. Sarajlic, X. Li, and F. Tufvesson, "Deep convolutional neural networks for massive MIMO fingerprint-based positioning," in *Proc. IEEE Intl. Symp. Personal, Indoor, Mobile Radio Commun.*, Oct. 2017, pp. 1–6.
- [22] M. Arnold, J. Hoydis, and S. ten Brink, "Novel massive MIMO channel sounding data applied to deep learning-based indoor positioning," in *Intl. ITG Conf. Systems, Commun., Coding*, Feb. 2019, pp. 1–6.
- [23] P. Ferrand, A. Decurninge, and M. Guillaud, "DNN-based localization from channel estimates: Feature design and experimental results," in *Proc. IEEE Global Telecommun. Conf. (GLOBECOM)*, Dec. 2020, pp. 1–6.
- [24] M. Stahlke, T. Feigl, M. H. C. García, R. A. Stirling-Gallacher, J. Seitz, and C. Mutschler, "Transfer learning to adapt 5G AI-based fingerprint localization across environments," in *Proc. IEEE Veh. Technol. Conf. Spring (VTC-Spring)*, Jun. 2022, pp. 1–5.
- [25] E. Gönültaş, E. Lei, J. Langerman, H. Huang, and C. Studer, "CSI-based multi-antenna and multi-point indoor positioning using probability fusion," *IEEE Trans. Wireless Commun.*, vol. 21, no. 4, pp. 2162–2176, Apr. 2022.
- [26] A. Foliadis, M. H. Castañeda Garcia, R. A. Stirling-Gallacher, and R. S. Thomä, "Reliable deep learning based localization with CSI fingerprints and multiple base stations," in *Proc. IEEE Int. Conf. Commun. (ICC)*, May 2022, pp. 3214–3219.
- [27] X. Li, H. Al-Tous, S. E. Hajri, and O. Tirkkonen, "Covariance difference of arrival based fingerprinting localization," in *Proc. IEEE Veh. Technol. Conf. Spring (VTC-Spring)*, Jun. 2023, pp. 1–6.
- [28] G. Tian, I. Yaman, M. Sandra, X. Cai, L. Liu, and F. Tufvesson, "Deep-learning-based high-precision localization with massive MIMO," *IEEE Trans. on Mach. Learn. in Commun. and Netw.*, vol. 2, pp. 19–33, Nov. 2024.
- [29] P. Huang, O. Castañeda, E. Gönültaş, S. Medjkouh, O. Tirkkonen, T. Goldstein, and C. Studer, "Improving channel charting with representation-constrained autoencoders," in *Proc. IEEE Int. Workshop Signal Process. Advances Wireless Commun. (SPAWC)*, Aug. 2019, pp. 1–5.
- [30] E. Lei, O. Castañeda, O. Tirkkonen, T. Goldstein, and C. Studer, "Siamese neural networks for wireless positioning and channel charting," in *Proc. Allerton Conf. Commun., Contr., Comput.*, Sep. 2019, pp. 200–207.
- [31] J. Deng, O. Tirkkonen, J. Zhang, X. Jiao, and C. Studer, "Network-side localization via semi-supervised multi-point channel charting," in *Proc. Int. Wireless Commun. and Mobile Comput. (IWCMC)*, Jun. 2021, pp. 1654–1660.
- [32] Q. Zhang and W. Saad, "Semi-supervised learning for channel charting-aided IoT localization in millimeter wave networks," in *Proc. IEEE Global Telecommun. Conf. (GLOBECOM)*, Dec. 2021, pp. 1–6.
- [33] J. Deng, W. Shi, J. Hu, and X. Jiao, "Semi-supervised t-SNE for millimeter-wave wireless localization," in *Int. Conf. on Comput. and Commun. (ICCC)*, Dec. 2021, pp. 1015–1019.
- [34] I. Karmanov, F. G. Zanjani, I. Kadampot, S. Merlin, and D. Dijkman, "WiCluster: Passive indoor 2D/3D positioning using WiFi without precise labels," in *Proc. IEEE Global Telecommun. Conf. (GLOBECOM)*, Dec. 2021, pp. 1–7.
- [35] F. Euchner, P. Stephan, and S. t. Brink, "Augmenting channel charting with classical wireless source localization techniques," in *Proc. Asilomar Conf. Signals, Syst., Comput.*, Oct. 2023, pp. 1641–1647.
- [36] O. Esrafilian, M. Ahadi, F. Kaltenberger, and D. Gesbert, "Global scale self-supervised channel charting with sensor fusion," *arXiv preprint arXiv:2405.04357*, 2024.

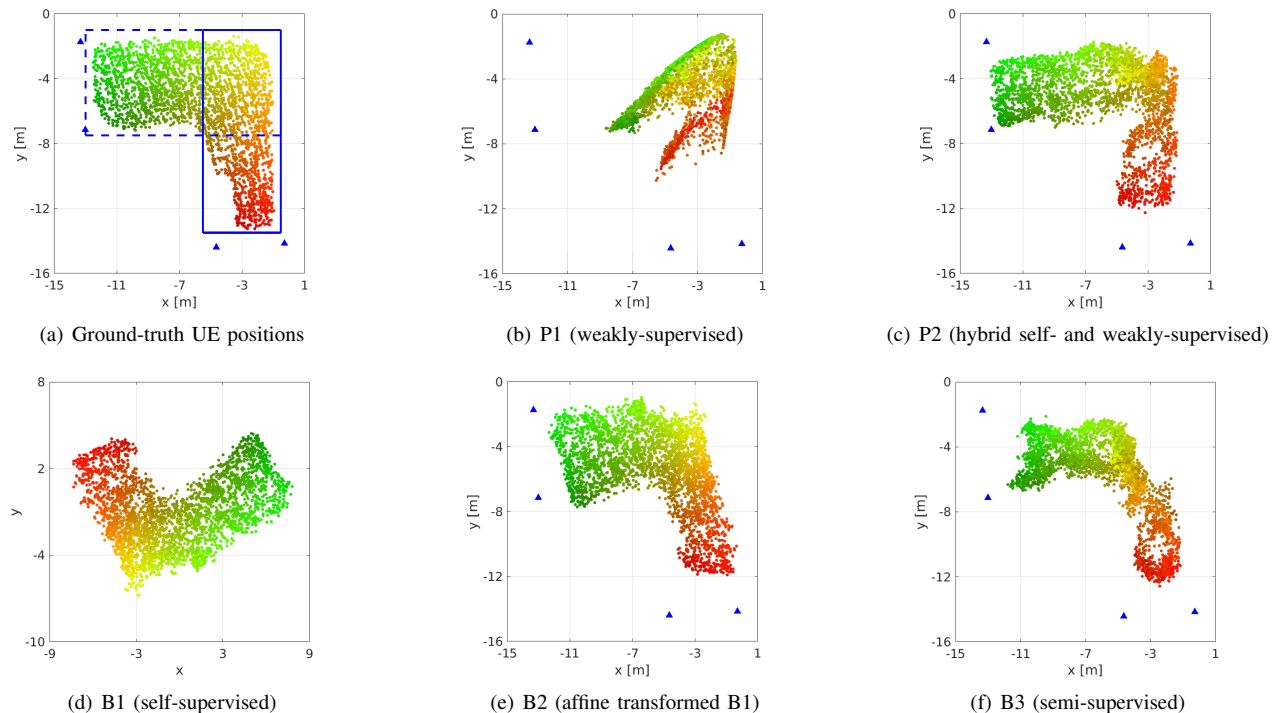


Fig. 7. Results for the measured indoor scenario: (a) ground-truth UE positions (green-to-red gradient colored area), AP positions (blue triangles), and the two LoS bounding boxes corresponding to the top and bottom APs (blue solid and dashed lines); and (b-f) the channel charts or positioning estimates for the proposed (P) and baseline (B) methods. Since the output of baseline B2 is in arbitrary coordinates, the AP positions are not shown in (d). The proposed method P2 achieves comparable results in real-world coordinates as the semi-supervised baseline B3 but without requiring known UE positions during training.

- [37] J. Pihlajasalo, M. Koivisto, J. Talvitie, S. Ali-Löytty, and M. Valkama, “Absolute positioning with unsupervised multipoint channel charting for 5G networks,” in *Proc. IEEE Veh. Technol. Conf. Fall (VTC-Fall)*, Nov. 2020, pp. 1–5.
- [38] M. Stahlke, G. Yammine, T. Feigl, B. M. Eskofier, and C. Mutschler, “Indoor localization with robust global channel charting: A time-distance-based approach,” *IEEE Trans. on Mach. Learn. in Commun. and Netw.*, Mar. 2023.
- [39] M. Stahlke, G. Yammine, T. Feigl, B. Eskofier, and C. Mutschler, “Velocity-based channel charting with spatial distribution map matching,” *arXiv preprint arXiv:2311.08016*, Nov. 2023.
- [40] P. Stephan, F. Euchner, and S. Ten Brink, “Angle-delay profile-based and timestamp-aided dissimilarity metrics for channel charting,” *IEEE Trans. Commun.*, Apr. 2024, early access.
- [41] L. van der Maaten, E. Postma, and J. van den Herik, “Dimensionality reduction: a comparative review,” *J. Mach. Learn. Research*, vol. 10, no. 1–41, 2009.
- [42] B. Rappaport, E. Gönültaş, J. Hoydis, M. Arnold, P. K. Srinath, and C. Studer, “Improving channel charting using a split triplet loss and an inertial regularizer,” in *Int. Symp. on Wireless Commun. Sys.s (ISWCS)*, Sep. 2021, pp. 1–6.
- [43] T. Yassine, L. L. Magoarou, S. Paquelet, and M. Crussière, “Leveraging triplet loss and nonlinear dimensionality reduction for on-the-fly channel charting,” in *Proc. IEEE Int. Workshop Signal Process. Advances Wireless Commun. (SPAWC)*, Jul. 2022, pp. 1–5.
- [44] X. Glorot and Y. Bengio, “Understanding the difficulty of training deep feedforward neural networks,” in *Proc. Thirteenth Int. Conf. Artificial Intelligence Stat.*, vol. 9, May 2010, pp. 249–256.
- [45] K. He, X. Zhang, S. Ren, and J. Sun, “Delving deep into rectifiers: Surpassing human-level performance on ImageNet classification,” in *IEEE Int. Conf. Comp. Vision (ICCV)*, Dec. 2015, pp. 1026–1034.
- [46] H. Al-Tous, P. Kazemi, C. Studer, and O. Tirkkonen, “Channel charting with angle-delay-power-profile features and earth-mover distance,” in *Proc. Asilomar Conf. Signals, Syst., Comput.*, Oct. 2022, pp. 1195–1201.
- [47] Á. Vathy-Fogarassy and J. Abonyi, “Graph-based clustering and data visualization algorithms,” in *Springer Briefs in Computer Science*, 2013.
- [48] J. B. Kruskal, “Multidimensional scaling by optimizing goodness of fit to a nonmetric hypothesis,” *Psychometrika*, vol. 29, no. 1, pp. 1–27, 1964.
- [49] C. Rajsiki, “A metric space of discrete probability distributions,” *Information and Control*, vol. 4, no. 4, pp. 371–377, 1961.
- [50] F. Euchner, M. Gauger, S. Dörner, and S. ten Brink, “A distributed massive MIMO channel sounder for “big CSI data”-driven machine learning,” in *Proc. Int. ITG Workshop on Smart Antennas (WSA)*, Nov. 2021.